Energy Advances

ROYAL SOCIETY OF CHEMISTRY

PAPER

View Article Online
View Journal | View Issue

Check for updates

Cite this: *Energy Adv.*, 2026, **5**, 408

Electroreduction of zirconia – a multi-step process

Christian Rodenbücher, *[a] Kiana Khosravani, [ab] Parham Shokouhi, [a] Kristof Szot, [c] Michał Pilch, [c] Heinrich Hartmann, [a] Dominik Wrana, [d] Franciszek Krok [d] and Carsten Korte [a]

Received 21st November 2025,
Accepted 27th February 2026

DOI: 10.1039/d5ya00338e

rsc.li/energy-advances

The phenomenon of electroreduction, or electrocoloration, in yttria-stabilised zirconia (YSZ) has garnered significant attention due to its dual role as a possible degradation mechanism in solid oxide electrolysers and as a beneficial effect during the flash sintering of ceramics with tailored properties. Despite extensive investigation over several decades, the precise mechanisms underlying the transformation of the transparent, purely ionic conductor YSZ into a black, mixed ionic-electronic conductor, and eventually into a metallic state, remain inadequately understood. In this study, we present a comprehensive analysis that integrates electrical characterisation during electroreduction with *in situ* microscopy and *ex situ* spectroscopy techniques. Our findings enable us to delineate three primary stages: a reversible electrocoloration associated with the development of blackening fingers, an accelerated electroreduction facilitated by the formation of mixed ionic-electronic conducting pathways between the anode and cathode, and a runaway-type process that induces morphological changes and filamentary phase transformations in the surface region.

Open Access Article. Published on 27 February 2026. Downloaded on 5/4/2026 10:17:25 AM.
This article is licensed under a Creative Commons Attribution 3.0 Unported Licence.

Introduction

Yttria-stabilised zirconia (YSZ) is known as a prototypical solid oxygen ion conductor and finds use, *e.g.*, as an electrolyte material in solid oxide cells (SOCs), which convert chemical energy stored, *e.g.*, as hydrogen (H_2) into electrical energy and *vice versa*.[1–3] Although YSZ, which crystallises in the cubic fluorite structure, is a highly stable material with demonstrated long-term applicability in solid oxide fuel cells, it may be susceptible to degradation effects when subjected to electric field gradients under reducing conditions, as may occur when SOCs operate in electrolyser mode (SOEC).[4,5] A future aim for next generation SOECs, is a further decrease of the operation temperature below 700 °C. This can be achieved when changing to ceria-based solid electrolytes, *e.g.*, gadolinium oxide doped cerium dioxide (GDC). Ceria-based materials are even more prone to electroreduction phenomena. Electroreduction effects are also pertinent to the flash sintering of ceramics and have been employed to prepare YSZ samples with controlled oxygen deficiency or even new rocksalt-type ZrO phases on the surface.[6–14]

To elucidate the fundamentals of this degradation mechanism, the electroreduction effect in YSZ has been extensively studied over recent decades.[15–20] Electroreduction experiments are typically conducted in a Hebb–Wagner geometry with an ion-blocking cathode and an oxygen-permeable anode.[21,22] These experiments have identified the development of a dark-coloured zone with a characteristic finger-like morphology extending from the cathode towards the anode, a phenomenon termed "electrocoloration" or "blackening". The finger-like morphology is the result of an instability phenomenon (self-amplification) due to the growth of a highly conducting product phase into the comparable low-conducting unreduced solid electrolyte phase.[21,23]

In general, when a YSZ sample is exposed to an electric field, oxygen ions migrate from the cathode to the anode. The cathode supplies the electronic charge carriers, leaving behind an oxygen vacancy-rich region with enhanced electronic conductivity due to reduced cation oxidation states.[21,24] Various analytical techniques have been employed to investigate the blackened region, concluding that the concentration of oxygen vacancies in these regions is significantly increased, leading to the formation of colour centres and the reduction of Zr from a +4 valence state to +3, +1, or even metallic Zr^0.[25–28]

In the present study, we aim to investigate the progression of electroreduction in YSZ single crystals at moderate

[a] *Institute of Energy Technologies (IET-4), Forschungszentrum Jülich GmbH, 52428 Jülich, Germany. E-mail: c.rodenbuecher@fz-juelich.de*
[b] *Institute of Energy Materials and Devices (IMD-3), Forschungszentrum Jülich GmbH, 52428 Jülich, Germany*
[c] *A. Chełkowski Institute of Physics, University of Silesia, 41-500 Chorzów, Poland*
[d] *Marian Smoluchowski Institute of Physics, Jagiellonian University, 30-348 Kraków, Poland*

© 2026 The Author(s). Published by the Royal Society of Chemistry

Open Access Article. Published on 27 February 2026. Downloaded on 5/4/2026 10:17:25 AM.
This article is licensed under a Creative Commons Attribution 3.0 Unported Licence.

temperatures of 400 °C under reducing vacuum conditions. We employ a combination of *in situ* microscopy and electrical characterisation, complemented by comprehensive spectroscopic *ex situ* analysis of YSZ single crystals electroreduced to various states. Special emphasis is placed on determining whether electrocoloration is primarily a bulk or surface phenomenon and on distinguishing between mild and heavy electroreduction.

Results and discussion

Electroreduction, on-top mounted electrodes

To illustrate the influence of different driving forces on the progression of electroreduction, degradation experiments are conducted at three different voltages: 200, 500, and 1000 V under vacuum conditions and a temperature of 400 °C. The voltages are chosen in order to obtain a full reduction in a reasonable time for the given sample and electrode geometry. Considering that the thickness of the solid electrolyte in SOEC operating around 1.5 V is in the range of 10–100 μm, a similar electric field would be present when using the selected voltages in our macroscopic model experiment. The current measured during electroreduction is presented in Fig. 1. It is evident that the reduction process is not constant, but rather three distinct regimes can be identified. Initially, the current increases slowly, resulting in an almost horizontal current–time curve in the double logarithmic representation of Fig. 1 (stage I). Subsequently, a significant increase in the current is observed for all three samples, indicating an acceleration of the electroreduction (stage II).

In the final stage of the experiment, a significant increase in current, exceeding two orders of magnitude, is observed, reaching the current compliance of 10 mA within a few minutes in a runaway-type manner for applied voltages of 500 and 1000 V (stage III). Upon reaching current compliance, the voltage is automatically reduced to maintain a constant current for an additional 30 min before being switched off. The rate of electroreduction is dependent on the applied voltage. Specifically, at 1000 V, the current compliance was achieved in 1.28 h, whereas at 500 V, it took 10.25 h. Conversely, at 200 V, the process remains in stage II and does not reach current compliance within the experimental duration of 7.8 days. Throughout the entire electroreduction experiment, the current increases by more than four orders of magnitude for samples that reached stage III, indicating a reduction in sample resistance from the GΩ range to the kΩ range.

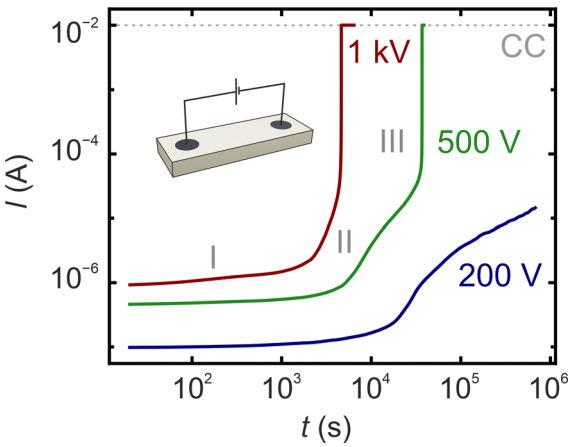

Fig. 1 Current as a function of degradation time measured during the electroreduction of three samples with different voltages. The inset displays the geometry of the sample setup. The Roman numerals mark the three electroreduction stages, and the current compliance (CC) is shown as a dashed line.

Progression of electro-colouration

Fig. 2 presents selected snapshots of the samples during the reduction process, obtained *via in situ* microscopy. Initially, the epi-polished single crystals are transparent and exhibit no colouration. During electroreduction, a finger-like reaction front of dark-red colour emerges from the cathode, progressing towards the anode. The morphology of the front is consistent across all three investigated voltages. The finger-like features of the reaction front are aligning with the electric field lines of the circular electrodes; however, the speed of progression is increasing with higher voltages. At the onset of electroreduction, the appearance of the electrode on the anode side changes from dark to shiny and reflective, which can be attributed to a roughening of the sputtered Pt electrode due to the electrochemical release of oxygen at the anode. Once the finger-like reaction front reaches the anode, the blackened region becomes more diffuse, and the colouration is intensified (second row of Fig. 2(a)–(c)). By comparing the optical images with the current–time characteristics in Fig. 1, one can correlate the arrival of the finger-like reaction front at the anode with the onset of accelerated electroreduction in stage II for all three investigated voltages (10 h for 200 V, 3 h for 500 V, and 70 min for 1000 V). As the electroreduction is progressing in stage II, the region of the sample between the electrodes turns deep black, with only the rims of the crystal remaining transparent. For samples treated at 500 and 1000 V, which reach stage III, the entire crystal turns black. Only very small regions at the rims of the crystal are retaining their transparency (for a detailed analysis of the onset of stage III, see Fig. 6).

To elucidate the progression of the reduction front at varying voltages, the colour of the optical images is analysed. The red, green, and blue (RGB) values of these images are converted into a grey-scale, and the average grey values of 14 profile lines, equally distributed with a separation of 0.4 mm between the anode and cathode, are calculated for all images recorded during the reduction period. The normalised results are presented as blackness values in Fig. 2d. The shapes of the curve indicate, firstly, the increasing blackening speed with rising voltage and, secondly, the progression of the blackening from cathode to anode, with regions near the cathode (purple) exhibiting increased blackness values earlier than those near the anode (red). The most pronounced increase in blackness is associated with stage I, when the initial blackening front traverses the crystal. In stage II, the differences between regions

Open Access Article. Published on 27 February 2026. Downloaded on 5/4/2026 10:17:25 AM.
This article is licensed under a Creative Commons Attribution 3.0 Unported Licence.

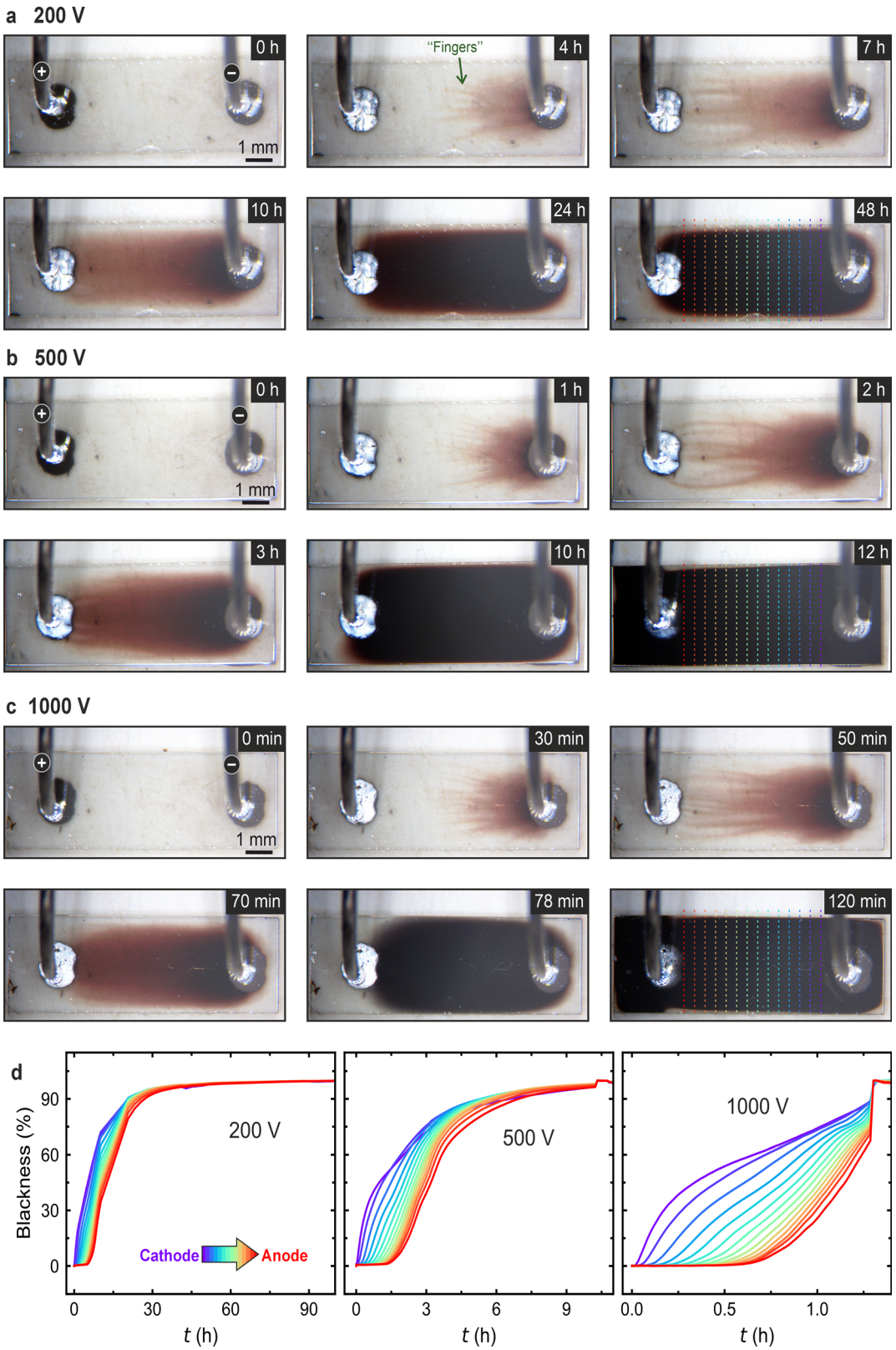

Fig. 2 *In situ* optical microscopy obtained during electroreduction of YSZ single crystals kept at 400 °C under different voltages (a) 200 V, (b) 500 V, (c) 1000 V (see also supplementary video). (d) Progression of the blackness as a function of time calculated for 14 equidistant points between anode and cathode marked by dashed lines.

© 2026 The Author(s). Published by the Royal Society of Chemistry

Open Access Article. Published on 27 February 2026. Downloaded on 5/4/2026 10:17:25 AM.
This article is licensed under a Creative Commons Attribution 3.0 Unported Licence.

diminish, and the blackness increases more uniformly. Upon reaching the runaway-like current jump, the blackness values surge to their maximum. Subsequently, a slight reduction in blackness value is observed, potentially related to surface restructuring, as it will be discussed below.

Optical properties of electro-coloured samples

The properties of the electroreduced samples are investigated using UV-VIS spectroscopy. The transmission spectra are shown in (Fig. 3a). The unreduced reference crystal (grey line) exhibits a high transmission up to above 3 eV, reflecting the optical transparent nature of YSZ single crystals. The band gap, as determined by the Tauc method, is 4.64(2) eV.[29] The transmission of the three electroreduced samples from Fig. 2, which appear black to the naked eye, is significantly suppressed in the visible range (blueish curves in Fig. 3a). Only at low energies below 2–1.5 eV, the onset of increased optical transmission can be detected. Among these samples, the one electroreduced at 200 V exhibits the highest transmission, which is reasonable as it did not reach stage III. The sample electroreduced at 500 V has the lowest transmission, while the ''1000 V'' sample shows a slightly higher transmission in the infrared range.

To further elucidate the change in optical properties upon reduction, an additional sample is investigated. It is electroreduced at 1000 V, but the process is halted after 55 min at a current of 2.4×10^{-5} A, when the sample has only reached stage II and has not yet turned completely black. Instead, it retains a reddish colouration, darker at the cathode side than at the anode side, as depicted in the micrograph marked with ''1 kV short'' in Fig. 3b. The transmission spectra of this sample measured at different positions between anode and cathode, as marked by the dashed lines, are presented as rainbow curves in Fig. 3a. The illuminated areas have a width of approximately 0.5 mm. For the curves obtained from the reddish parts of the sample, the transmission reaches a local minimum around 2.5 eV, subsequently increases to a local maximum between 3 and 4 eV, and then declines to zero above 5 eV. Below 2 eV, the transmission increases significantly, eventually reaching the original values of the reference crystal below 1.5 eV. Consequently, light with wavelengths above 600 nm is still transmitted in substantial amounts, rendering the sample reddish in appearance. It is evident that the overall transmission decreases from the anode towards the cathode. This reflects the temporal progression of electrocoloration. In order to illustrate this progression, the transmission value at 2.54 eV corresponding to blue/green light is plotted as a blue curve in Fig. 3b. The band gap of the transmission spectra as calculated by the Tauc method is shown as a green curve in Fig. 3b. For all measured positions, the band gap is slightly higher than that of the reference sample (dashed line). The observed increase in the band gap following the reduction of YSZ has been previously documented and is attributed to the formation of doubly occupied oxygen vacancies acting as *F* centres.[28] Starting from the cathode, the band gap increases slightly at first and then decreases significantly close to the anode. This illustrates again that the anode region is not that strongly reduced and hence the band gap value is closer to the reference.

Reversibility, electrochemical re-oxidation

In the subsequent analysis, we want to focus on the initial electrocoloration occurring in stage I and to assess the possible reversibility of this process. Thus, an electroreduction experiment is conducted, wherein the polarity is periodically reversed. As depicted in Fig. 4a, an initial voltage of +200 V is applied for one hour, followed by a zero voltage for another hour. Subsequently, a voltage of −200 V is applied for one hour, followed by another hour of 0 V, and a final hour with a voltage of +200 V. During the voltage application, the current (Fig. 4b) is in the range of 10^{-7} A, comparable to stage I of the long-term experiment in Fig. 1. When the voltage is set to zero after each high-voltage application, a reverse current in the range of 10^{-9} A is detectable, which gradually decays over time. This suggests that a stoichiometry polarisation is established during electroreduction, resulting in an electromotive force that generates the reverse current when the electrodes are short-circuited.

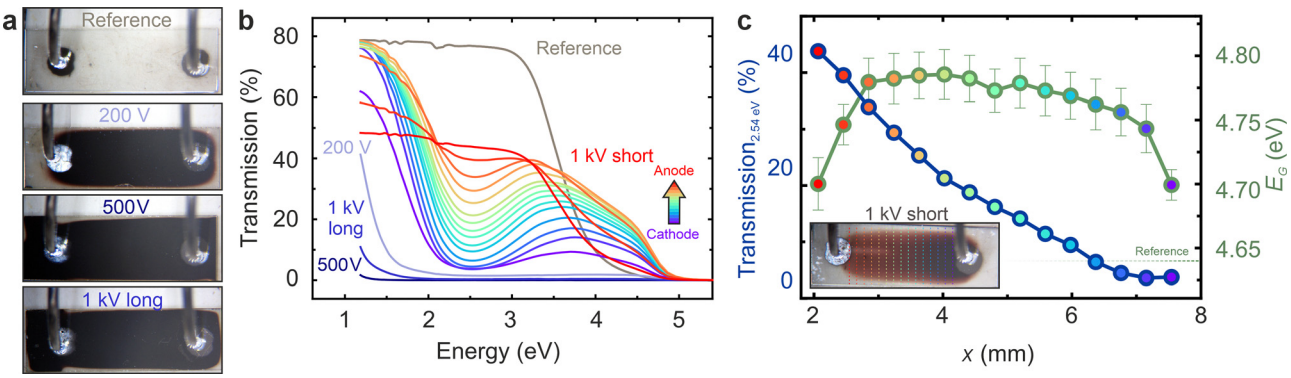

Fig. 3 UV-VIS investigations of YSZ samples in various reduction states. (a) Optical micrographs. (b) Transmission spectra; the curves displayed in rainbow colours correspond to spatially-resolved investigations of a sample, whose electroreduction was stopped at the onset of stage II (''1 kV short''). (c) Progression of the transmission at 2.54 eV and calculated band gaps for different positions between cathode and anode of the ''1 kV short''' sample as marked by the dashed lines in the inset micrograph.

Open Access Article. Published on 27 February 2026. Downloaded on 5/4/2026 10:17:25 AM.
This article is licensed under a Creative Commons Attribution 3.0 Unported Licence.

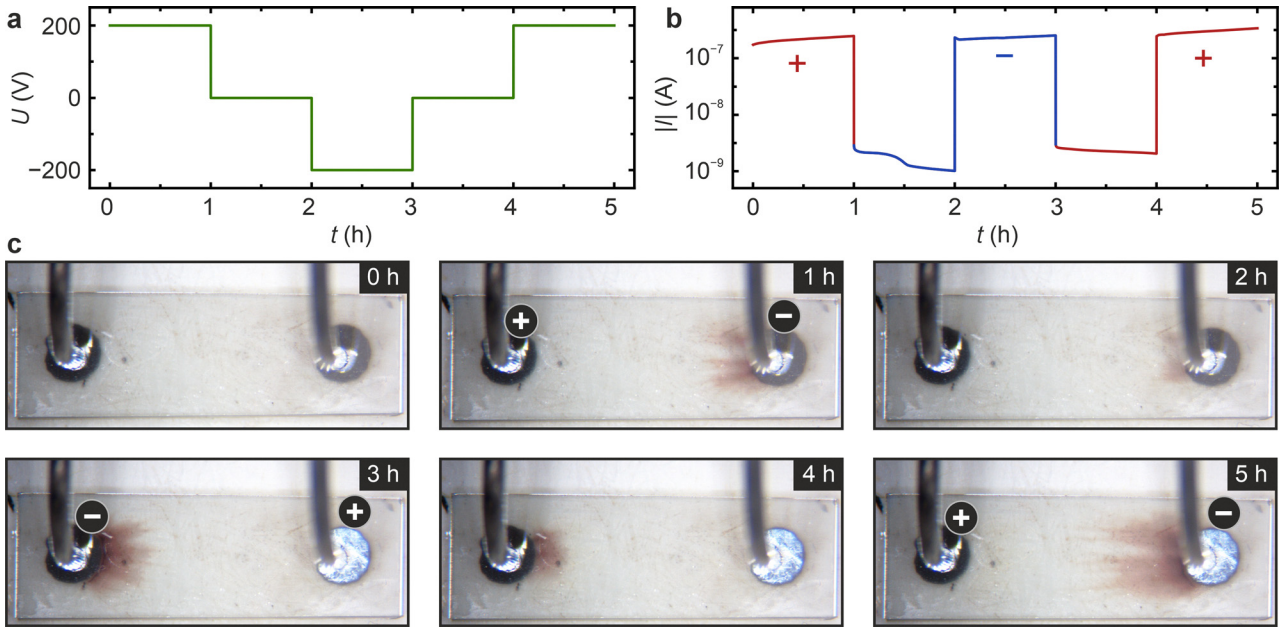

Fig. 4 Electroreduction at 200 V with alternating polarity performed at 400 °C under vacuum conditions. (a) Applied voltage profile, (b) absolute value of the measured current in a logarithmic scale (positive and negative values are marked in red and blue, respectively), (c) micrographs obtained by *in-situ* optical microscopy during the electroreduction (see also supplementary video).

The examination of the micrographs obtained by optical microscopy during the process (Fig. 4c) reveals that after one hour of applying a positive voltage, blackening fingers emerge from the electrode on the right side, acting as a cathode, see Fig. 2a. When the voltage is subsequently set to zero, the fingers partially retract, leaving only a slight reddish colouration near the cathode (2 h). Upon application of the voltage with negative polarity, the colouration at the right electrode (former cathode, now the anode) completely disappeared, and the development of blackening fingers at the opposite electrode commenced (3 h). Additionally, on the left electrode, the blackening fingers partially retract after short-circuiting (4 h) and disappear upon applying the opposite voltage (5 h).

After 5 h, corresponding to the second application of a positive voltage, the blackening fingers on the right electrode appear again at approximately the same position as after 1 h, but they extend approximately twice as far towards the anode, which indicates a more pronounced reduction than after the initial hour of electroreduction. This observation suggests that, although the optical properties near the electrode revert to their original transparent state, some irreversible effects occur. Conducted under vacuum conditions, the experiment results in continuous oxygen loss from the sample during polarisation with both polarities. Consequently, the overall oxygen vacancy concentration during the second positive polarisation is higher than during the first, potentially accounting for the more effective second electroreduction. Additionally, one may consider that during the first polarisation, some irreversible nanoscale effects might occur, such as clustering of oxygen vacancies or a complex interaction between vacancies as point defects and extended defects like dislocations. Nonetheless, it can be concluded that the electrocoloration effect in stage I is reversible, and a macroscopic phase transformation is not anticipated at this stage. After heavy electroreduction in stages II and III instead, a restoration of the transparency is not observed when reversing the voltage polarity, as the nature of charge carriers of the observed current changes from ionic to electronic during electroreduction. Furthermore, the experiment is conducted under vacuum conditions and there are no significant amounts of oxygen available, which could lead to a full reoxidation. Hence, stages II and II can be regarded as electrochemically irreversible under the given experimental conditions.

Tomographic investigations

Our previous investigations on the electroreduction of solid oxides with low oxygen conductivity, such as $SrTiO_3$ and TiO_2, have demonstrated that reduction occurs only in the dislocation-rich surface region when metallic filaments form along the dislocation network.[30,31] In these materials, the surface colour was significantly darker than that of the bulk, indicating that electroreduction and colouration are confined to the surface region. Similarly, for YSZ, it has been observed that dislocations beneficially influence ionic transport properties.[32–35] Therefore, the question arises whether electrocoloration in YSZ, a material with a significantly higher ionic conductivity than $SrTiO_3$ and TiO_2, is a surface or bulk phenomenon. To address this issue, we section the two slightly electroreduced samples, ''1 kV short'' and ''200 V'' (the same samples as in Fig. 3), along their long axis using a diamond saw to prepare cross-sections. The micrographs taken by optical microscopy of these cross-sections are depicted in Fig. 5a and b. Colouration occurs not only in the surface region but also

© 2026 The Author(s). Published by the Royal Society of Chemistry

Open Access Article. Published on 27 February 2026. Downloaded on 5/4/2026 10:17:25 AM.
This article is licensed under a Creative Commons Attribution 3.0 Unported Licence.

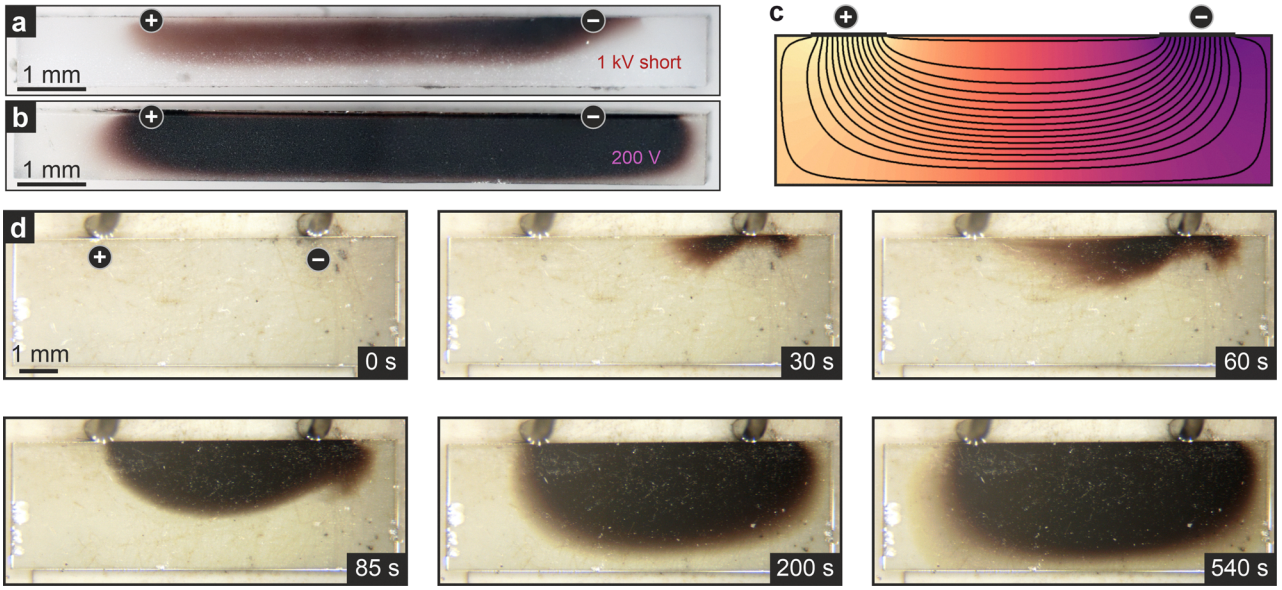

Fig. 5 Progression of blackening in the interior of the sample. (a) *Ex situ* cross-section of the sample electroreduced at 1000 V for short time (*cf.* Fig. 3) and (b) at 200 V for long time. (c) Illustration of the potential distribution and current paths simulated by the finite element method. (d) Micrographs obtained by *in situ* optical microscopy during electroreduction at 1000 V with electrodes deposited on the top edge side of the crystal.

penetrates deeply into the bulk. For the sample after short electroreduction (Fig. 5a), the blackening is more pronounced near the cathode than the anode, consistent with the top-view image in Fig. 3. The "200 V" sample in Fig. 5b exhibits a dark black colour between the electrodes. Here, electrocoloration occurs not only between the electrodes, but it is also extended to the region between the cathode and the right edge of the sample. To elucidate the specific configuration of colouration in the out-of-plane direction, the potential distribution and current pathways are simulated utilising the electrostatic finite element method. The results, depicted in Fig. 5c, demonstrate that the particular geometry of the electrodes, positioned on the top side of the sample, induces curved electric field lines extending from the surface towards the bulk and returning. For this simulation, a constant resistivity and permittivity of the material are assumed. Hence, the calculated potential distribution only describes the situation at the start of electroreduction. With progression electroreduction, the resistance of the area close to the cathode gets significantly lower, which would lead to a non-linear drop of the potential between anode and cathode. Assuming that the colouration is directly related to the reduction state, the progression of the optical transmission in Fig. 3b could serve as a first approximation of the potential drop. Hence, one can expect that during the electroreduction, a "virtual cathode" moves through the sample, shifting the position of maximum potential drop more and more to the anode.

Electroreduction, laterally mounted electrodes

A post-mortem analysis through sample sectioning can only provide information regarding the final colouration/reduction state. Thus, an additional experiment is conducted to observe the out-of-plane progression of the blackening process *via in situ* optical microscopy. Consequently, the electrode geometry is rotated by 90° and the Pt electrodes are deposited on the smaller side of the sample. The progression of electrocoloration at a voltage of 200 V is illustrated in Fig. 5d. The rate of electrocoloration is significantly faster than that observed in the standard geometry (Fig. 2a), attributable to the increased current density. Initiating at the cathode, the blackening fingers extend towards the left side (towards the anode) as well as the right side, which is anticipated due to the curved course of the electric field lines. However, in the region directly beneath the electrode, the rate of blackening progression is slower, presumably due to distortions in the electric field. This may be caused by a locally insufficient contact of the electrode to the surface, inhomogeneities resulting from an (accidental) deposition of Pt on the top surface during preparation or internal crystallographic defects at or below the surface. As the electroreduction progresses, the shape of the colouration becomes more uniform and generally aligns with the expected configuration of the electric field lines. Thus, it can be concluded that the electrocoloration in stages I and II is a bulk effect, with its shape primarily determined by the electric field determined by the chosen electrode geometry.

Identification of heavily reduced regions

Finally, attention is directed to the transformations occurring in stage III, where substantial electroreduction takes place. Previous nanoscale investigations have indicated that during this stage, the local evolution of regions with significant oxygen deficit in the cathode region, leading to crystallographic phase transformations, can be anticipated.[27] As the samples appear completely black under optical microscopy (Fig. 2), the surface is analysed using confocal Raman microscopy. The Raman maps in Fig. 6a, c, and d are generated by plotting the intensity

Open Access Article. Published on 27 February 2026. Downloaded on 5/4/2026 10:17:25 AM.
This article is licensed under a Creative Commons Attribution 3.0 Unported Licence.

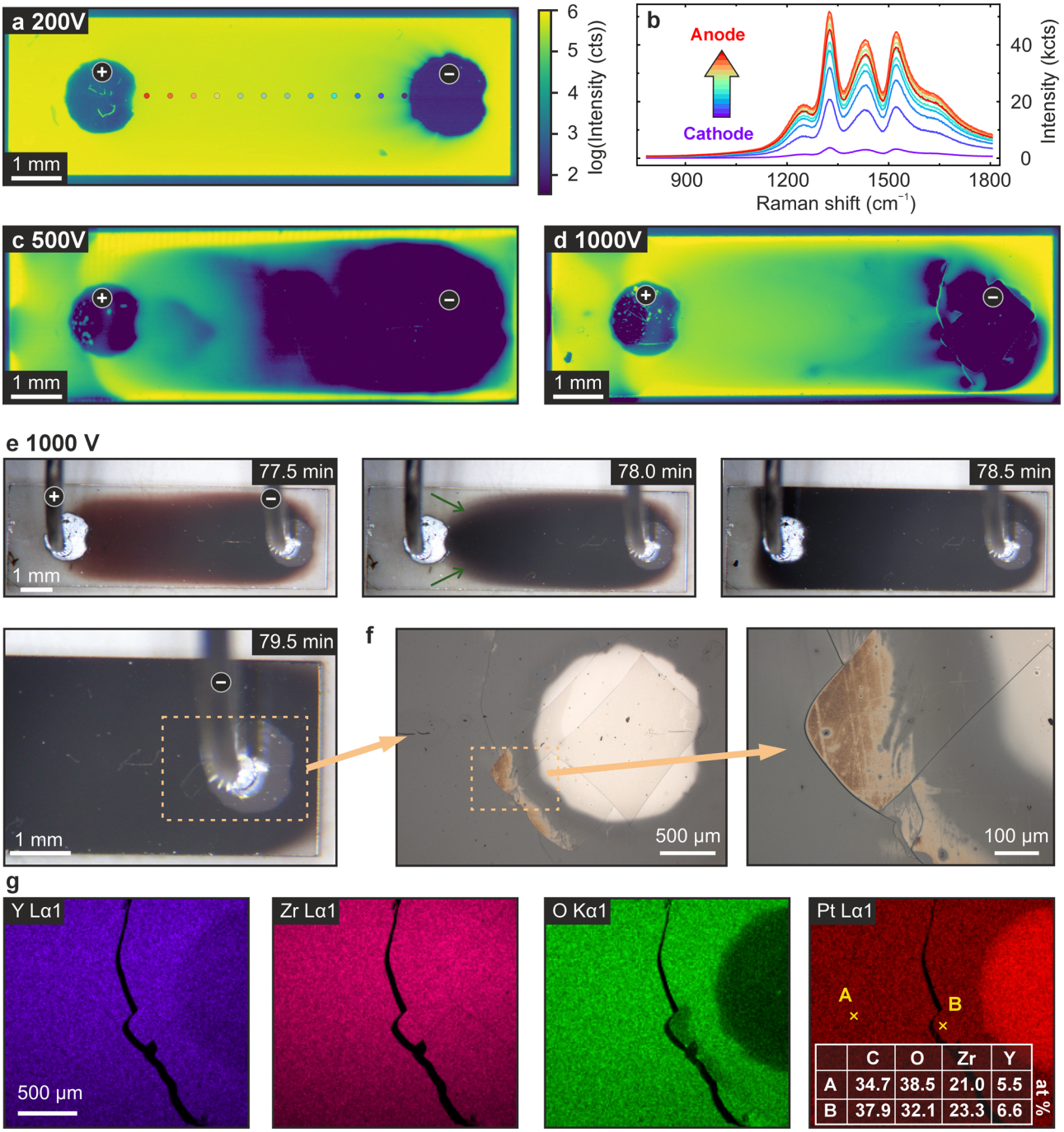

Fig. 6 Analysis of the features appearing on the surface upon prolonged electroreduction using various techniques. (a)–(d) *Ex situ* Raman spectromicroscopy (1527 cm^{-1}) of the samples treated at 200, 500 and 1000 V (*cf.* Fig. 2) with (b) selected spectra extracted from the positions marked with white dots in (a). (e) Micrographs of the sample reduced at 1000 V obtained by *in situ* optical microscopy, focusing on the time interval with the onset of the surface transformations. The cathode region is depicted in higher magnification, using *ex situ* reflected light microscopy. (g) EDX mapping of Y, Zr, O and Pt, tabulated atomic concentrations at two representative points A and B.

of the peak located at 1527 cm^{-1}, a characteristic high-intensity peak of cubic YSZ (*cf.* dataset R040142 in the RRUFF database[36]). In Fig. 6b, the high-frequency spectra for 12 points between the anode and cathode of the sample electroreduced at 200 V are presented as an example. It is evident that the intensity of the spectra diminishes towards the cathode, where the highest degree of reduction is anticipated. Since the Raman effect depends on the polarisability of a material, its suppression is expected when an increased number of electronic charge carriers is present upon reduction. For the "200 V" sample, which has only reached stage II of electroreduction, a significant suppression of Raman intensity can only be observed close to the

© 2026 The Author(s). Published by the Royal Society of Chemistry

Open Access Article. Published on 27 February 2026. Downloaded on 5/4/2026 10:17:25 AM. This article is licensed under a Creative Commons Attribution 3.0 Unported Licence.

cathode. For the stage III samples after electroreduction at 500 and 1000 V (Fig. 6c and d), a marked suppression of the Raman intensity is observed. In the ''500 V'' sample, a substantial region exhibiting minimal Raman intensity extends from the cathode towards the anode, encompassing nearly half of the sample. This region displays a rather inhomogeneous, meander-like structure, potentially indicative of filament formation, as previously documented.[27] In the ''1000 V'' sample, the area of significantly reduced Raman intensity is more localised at the cathode, although some cracks are evident. This suggests that considerable strain, accumulated during the runaway process of stage III, is culminating in the rupture of extended filament formation. In both instances, it can be concluded that the evolution of the heavily reduced region is less homogeneous compared to the initial electrocoloration process of stage I. The abrupt increase in current during stage III leads to the development of filamentary regions with elevated electronic conductivity, which in turn modify the distribution of the electric field in their vicinity.

Surface transformation upon heavy electroreduction

To further examine the runaway process in stage III, selected snapshots from the measurement depicted in Fig. 2c are presented in Fig. 6e. In the left micrograph, after 77.5 min of electroreduction, the sample remains in stage II, characterised by a reddish colouration that intensifies towards the cathode. By 78 min, the entire area between the electrodes turns black. However, near the anode, some regions of the previous reddish colouration revert to transparency (indicated by green arrows). This suggests a redistribution of oxygen vacancies and a channelling of the current. It can also be observed that during this process, blackening bubbles move through the sample, in particular at the rim of the sample (see supplementary video). After 78.5 min, the blackening extends further, eventually covering the entire sample (*cf.* ''120 min'' in Fig. 2c). A magnified view of the cathode region at 79.5 min reveals that crack formation had already occurred by this time. Nevertheless, the sample remained sufficiently conductive to carry a current of 10 mA until the experiment's conclusion.

The cathode region is further analysed using *ex situ* optical microscopy (Fig. 6f). It is evident that, in proximity to the cracks in the cathode region, the surface undergoes a significant transformation, resulting in the emergence of a new morphology. Subsequently, EDX measurements are conducted on the same region. The element distribution maps in Fig. 6g indicate that there are only a few macroscopic inhomogeneities in chemical composition. However, in the region exhibiting a notable change in surface morphology in Fig. 6f, a significant oxygen deficiency is detectable in the green panel in Fig. 6g (It should be noted that the crack, previously visible in optical microscopy, has enlarged due to mechanical stress during the transfer to the EDX sample holder).

The atomic concentrations determined by EDX are displayed in the inset table of Fig. 6g. It is evident that the oxygen content in the region exhibiting a new morphology (B) is markedly lower than in the adjacent region (A). The calculated O/Zr ratio for the surrounding area is 1.83, whereas in the heavily transformed region, it is 1.37. This finding corroborates the presence of significant oxygen nonstoichiometry in the region with new morphology, which results in the accumulation of strain and the emergence of new oxygen-deficient phases, as previously demonstrated in our earlier publication.[27]

Surface electronic structure and composition

To further investigate the chemical composition and electronic structure of the electroreduced samples, X-ray photoelectron spectroscopy is conducted. The core lines of Zr, Y, O, C and the valence band region of the ''100 V'', ''200 V'' and ''1000 V'' samples, measured in an area close to the cathode, are depicted in Fig. 7. The sample electroreduced at 200 V exhibits a doublet in the Zr3d and Y3d regions, indicating the presence of only the original valences Zr^{4+} and Y^{3+}. The O1s line displays a prominent peak associated with lattice oxygen and an additional shoulder peak at higher energy, attributed to surface contamination. Despite the electroreduction experiment being conducted under UHV conditions, the heating temperature of 400 °C was insufficient to eliminate organic contamination from the surface. Additionally, the sample was transported under ambient conditions from the electroreduction setup to the XPS chamber, potentially leading to further adsorption of organic contaminants from the air. Consequently, the C1s spectrum reveals a distinct peak related to C–C bonds (it should be noted that a thermal treatment of the sample in the XPS chamber was intentionally omitted in order to circumvent the occurrence of additional surface reactions, *e.g.*, due to thermal reduction). The valence band spectrum (VB) indicates the absence of occupied states near the Fermi energy (dashed line in Fig. 7), confirming that the surface remained in a semiconducting or insulating state. This observation is consistent with the conclusion that the ''200 V'' sample has only reached stage II, and extensive electroreduction did not occur.

In contrast, the XPS spectra of the samples electroreduced at 500 and 1000 V exhibit fundamentally different characteristics. For both samples, a new doublet at a lower binding energy in the Zr3d spectrum emerges, revealing the presence of at least one new Zr state with lower valence. According to Caspers *et al.*, this additional doublet could correspond to Zr^{2+} or even metallic Zr^0.[37] Using micro-spectroscopy, Luerßen *et al.* also identified additional doublets in the Zr3d line following electroreduction. They attributed them to Zr^{3+}, Zr^{1+}, and Zr^0.[25] The Y3d line of the ''500 V'' sample also exhibits an additional doublet at lower binding energy, confirming a partial reduction of Y. This additional doublet is absent in the spectrum of the ''1000 V'' sample, which can be attributed to the previously established conclusion that the surface of the sample is not that extensively reduced on a global scale due to a more pronounced localisation of the electroreduction related to crack formation.[27] In the O1s line, the second component at higher binding energy is notably larger for both samples. However, for the ''500 V'' sample, an additional minor component is present at an even higher binding energy of approximately 533 eV. In the carbon line of both high-voltage samples, four additional peaks are observed post-electroreduction, two at higher and two

Open Access Article. Published on 27 February 2026. Downloaded on 5/4/2026 10:17:25 AM.
This article is licensed under a Creative Commons Attribution 3.0 Unported Licence.

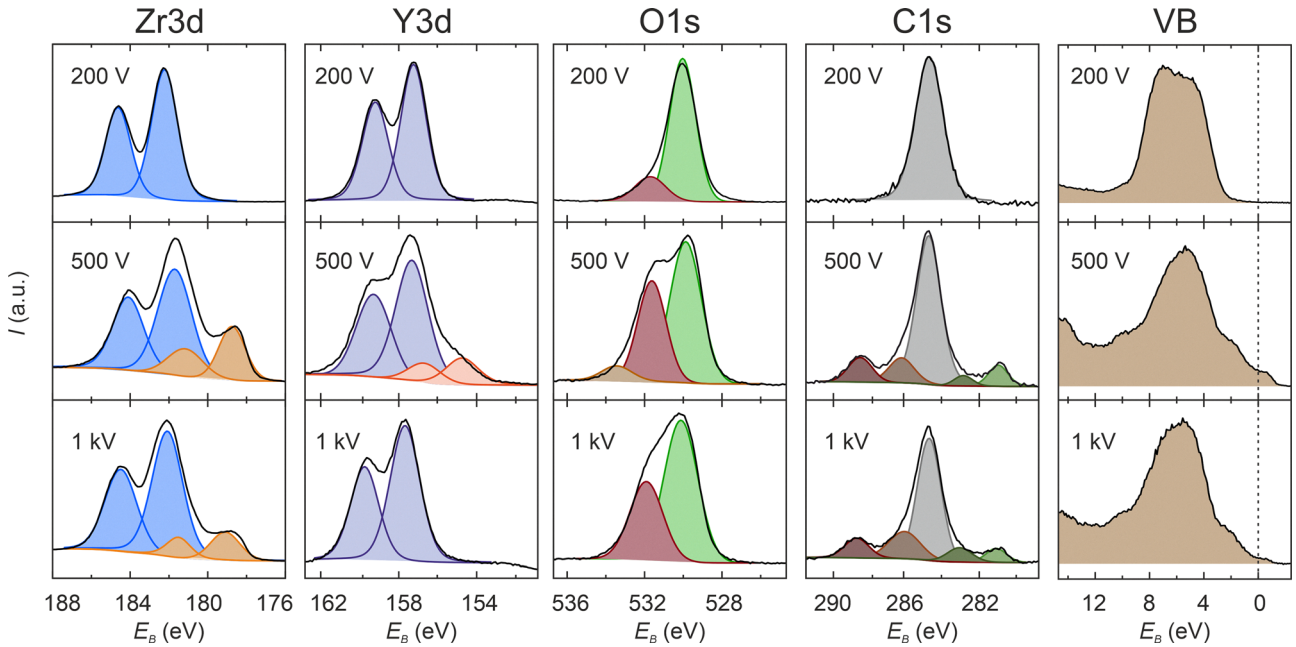

Fig. 7 XPS analysis of the electroreduced samples. Valence band (VB) region and core lines with deconvolution obtained by peak fitting.

at lower binding energies than the main C–C peak. The distinct peak at approximately 281 eV is indicative of carbides, suggesting a reaction between the adsorbed carbon and the solid oxide surface, resulting in the formation of ZrC or YC. Furthermore, the emergence of additional peaks in the C1s spectrum implies the formation of more complex carbon compounds.

The valence band spectrum, depicted in Fig. 7, exhibits a markedly different appearance following high-voltage electroreduction. Occupied states at the band gap are detectable in both spectra, with greater intensity for the "500 V" sample compared to the "1000 V" sample, indicating a local insulator–metal transition on the surface. The potential origins of this metallicity may include the formation of zirconium suboxides with metallic conductivity and the development of highly conductive carbides. This is corroborated by the atomic concentrations estimated from the core line spectra intensities shown in Fig. 8. The oxygen concentration in the high-voltage samples is significantly lower than in the "200 V" sample, while the carbon content is considerably higher. This suggests that upon heavy electroreduction, YSZ is reduced to yttrium–zirconium suboxides or metallic Zr and Y, which subsequently react with carbon to form carbides. It is anticipated that the suboxides are formed during the runaway-type electroreduction in stage III, while the subsequent formation of carbides may occur post-experiment, when the highly reduced sample is exposed to air prior to its introduction into the XPS measurement chamber. Similar effects have been observed in oxygen-deficient HfO_{2-x} thin films, which reacted with carbon compounds to form HfC during heating under UHV conditions.[38] The abrupt increase in current during stage III suggests the formation of highly conductive or even metallic filaments in the surface or subsurface region during this process. However, after reaching the current compliance and cooling the sample to room temperature, the bulk of the sample does not exhibit global metallic behaviour but rather semiconducting properties. It is important to consider that the distance between the electrodes in our chosen geometry is quite large, and the current is limited to 10 mA. Hence, it could be expected that an increase in the current density by decreasing the electrode distance or increasing the current could turn the whole sample into the metallic state, which is a promising prospect for future research.

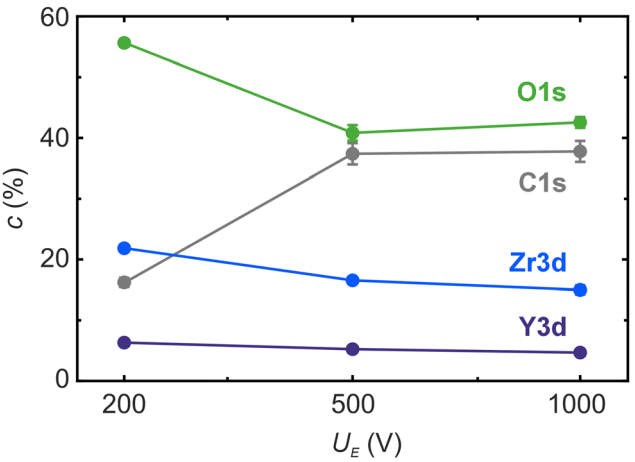

Fig. 8 Atomic concentration of the elements O, C, Zr, and Y obtained by XPS core line analysis for different electroreduction voltages U_E.

Experimental

Epi-polished single crystals of YSZ with a (100) orientation, measuring 3.3 mm × 10 mm × 1 mm and containing a nominal

© 2026 The Author(s). Published by the Royal Society of Chemistry

Open Access Article. Published on 27 February 2026. Downloaded on 5/4/2026 10:17:25 AM. This article is licensed under a Creative Commons Attribution 3.0 Unported Licence.

Y content of 8 mol%, are utilised (Mateck, Germany). Platinum electrodes, approximately 30 nm thick, are deposited *via* plasma sputtering using a shadow mask. The centre-to-centre distance of the electrodes, each with a diameter of 1.5 mm, is 7 mm. This results in a minimum anode–cathode distance of 5 mm. The electrodes are located on the top side of the crystals to enable sufficient electrical contact with the clamps. This geometry establishes a mainly in-plane current flow, enabling the differentiation of surface and bulk effects. Electroreduction is conducted under vacuum conditions ($p < 10^{-5}$ mbar) by applying voltages in a two-probe configuration at a temperature of 400 °C; for further details, refer to Rodenbücher *et al.*[27] During the electroreduction process, the current is monitored, and optical images of the samples are captured using a digital camera attached to an optical microscope (Kern, Germany). *Ex situ* optical microscopy is performed in reflection mode (Zeiss, Germany). Energy-dispersive X-ray (EDX) analysis is conducted using scanning electron microscopy (Zeiss, Germany) after sputtering a 2 nm gold layer on the samples to prevent charging effects. The potential and field distribution are simulated in a two-dimensional electrostatic setup employing the finite element method (Ansys, USA). Raman spectromicroscopy is performed by scanning the sample with a focused 785 nm diode laser and analysing the scattered light with a diffraction spectrometer using a confocal microscope (Renishaw, UK). The optical properties are analysed using a UV-VIS spectrometer in transmission geometry (VWR, USA). X-ray photoelectron spectroscopy is conducted *ex situ* at room temperature and under ultra-high vacuum (UHV) conditions using Al Kα radiation and an electron gun for charge compensation. The core level spectra are simulated using the Multipak software (Physical Electronics, USA).

Conclusions

We have presented a detailed microscopic and spectroscopic investigation of the processes involved in the electroreduction of YSZ single crystals subjected to high electric field gradients under reducing conditions. In this Hebb–Wagner type configuration, oxygen ions migrate from the cathode towards the anode, where they are released from the sample as oxygen gas. Conducted under vacuum conditions, the cathode is effectively blocking for oxygen incorporation. Consequently, a stoichiometry polarisation occurs, characterised by an increase in oxygen vacancies at the cathode side and an overall reduction in oxygen content, transforming the solid oxide from a purely ionic to a mixed ionic-electronic conductor. Our findings delineate three primary stages in this transformation:

- Stage I: A blackening front with finger-like morphology extends through the crystal from the cathode, primarily aligning with the electric field lines and inducing a dark-red colouration due to the formation of electronic states in the band gap associated with oxygen vacancies. This colouration can be reversed to the original transparent state of YSZ through electro-oxidation.
- Stage II: Upon the blackening fingers reaching the anode, a marked acceleration of the electroreduction process occurs, resulting in a macroscopic homogeneous blackening between the electrodes, manifesting as a dark-brown to black colouration. This blackening develops not only on the surface but also within the crystal's interior, indicating that the electrocoloration of YSZ is a bulk phenomenon.
- Stage III: The current rapidly increases by several orders of magnitude in a runaway manner until the predefined experimental current compliance is reached. Locally, new morphological features and crack formation on the surface are observed, associated with irreversible phase transformations of YSZ towards yttrium–zirconium suboxides or even metallic Y and Zr. This surface is highly reactive, forming metal carbides in the presence of organic adsorbates.

It is noteworthy that the electrocoloration in the first stages appears to be a bulk phenomenon, while the transformation into a highly conducting and eventually into a metallic state is an inhomogeneous filamentary effect, which takes place in the surface layer. Hence, it can be expected that extended defects such as dislocations, which *per se* have a higher ionic conductivity than the bulk,[32–35] play a decisive role during the insulator–metal transition induced by heavy electroreduction.

Our results suggest that the electroreduction of YSZ, as a prototype oxygen ion-conducting solid oxide, is a complex process with sequential phenomena. Thus, the transformation of the sample can be modulated by adjusting the voltage, current density, and electroreduction time between reversible and irreversible states. This provides not only insights into degradation phenomena in solid oxide electrolysis cells but also offers the potential to tailor solid oxide surfaces with customised electronic or catalytic properties through a technologically straightforward electrochemical process. As transient electrochemical driving forces are present during synthesis methods such as flash sintering or spark plasma sintering, either intentionally or as a result of the process, it is likely that strongly reduced phases form temporarily during compaction and are subsequently reoxidised. Furthermore, our results could pave the way for producing solid oxide ceramics with electrical properties ranging from insulating to metallic, which can be adjusted *via* electroreduction.

Author contributions

Conceptualisation: CR, MP, KS, FK, CK; data curation: CR; formal analysis: CR, KK, PS; funding acquisition: FK, CK; investigation: CR, KK, PS, MP, DW; methodology: CR, KS, DW, FK, CK; visualisation: CR, KK, PS; writing – original draft: CR; writing – review & editing: CR, KK, PS, MP, KS, HH, DW, FK, CK.

Conflicts of interest

There are no conflicts to declare.

© 2026 The Author(s). Published by the Royal Society of Chemistry

Open Access Article. Published on 27 February 2026. Downloaded on 5/4/2026 10:17:25 AM. This article is licensed under a Creative Commons Attribution 3.0 Unported Licence.

Data availability

The authors confirm that the data supporting the findings of the study are available within the article and the supplementary information (SI). Supplementary information: a supplementary video showing the progression of electroreduction is available. See DOI: https://doi.org/10.1039/d5ya00338e.

Acknowledgements

We gratefully acknowledge K. Klafki and A. Everwand for technical support. Open Access publication funded by the Deutsche Forschungsgemeinschaft (DFG, German Research Foundation)—Grant No. 491111487.

Notes and references

1 S. Zarabi Golkhatmi, M. I. Asghar and P. D. Lund, *Renewable Sustainable Energy Rev.*, 2022, **161**, 112339.
2 M. Singh, D. Zappa and E. Comini, *Int. J. Hydrogen Energy*, 2021, **46**, 27643–27674.
3 A. Risco-Bravo, C. Varela, J. Bartels and E. Zondervan, *Renewable Sustainable Energy Rev.*, 2024, **189**, 113930.
4 S. E. E. Wolf, F. E. E. Winterhalder, V. Vibhu, L. G. J. de Haart, O. Guillon, R.-A. Eichel and N. H. H. Menzler, *J. Mater. Chem. A*, 2023, **11**, 17977–18028.
5 L. Blum, L. G. J. de Haart, J. Malzbender, N. Margaritis and N. H. Menzler, *Energy Technol.*, 2016, **4**, 939–942.
6 X. Su, W. Li, D. Chen, S. Zhang, C. Lou, Q. Tian, J. Zhao and P. Zhao, *J. Adv. Ceram.*, 2024, **13**, 1881–1890.
7 F. Shi, B. Dashtbozorg, X. Li and H. Dong, *J. Mater. Res. Technol.*, 2024, **29**, 3759–3770.
8 A. Eqbal and T. Chakrabarti, *J. Eur. Ceram. Soc.*, 2023, **43**, 6260–6271.
9 N. Morisaki, T. Tokunaga, K. Kobayashi, A. Kodaira and T. Yamamoto, *Ceram. Int.*, 2022, **48**, 12091–12097.
10 K. Kobayashi, T. Yamamoto, K. Morita and T. S. Suzuki, *J. Ceram. Soc. Jpn.*, 2022, **130**, 172–179.
11 C. A. Grimley, A. L. Prette and E. C. Dickey, *Acta Mater.*, 2019, **174**, 271–278.
12 C. Bechteler and R. I. Todd, *Int. J. Appl. Ceram. Technol.*, 2025, **22**, e70011.
13 H. Charalambous, S. K. Jha, J. S. Okasinski and T. Tsakalakos, *Scr. Mater.*, 2021, **190**, 22–26.
14 J.-M. Lebrun, T. G. Morrissey, J. S. C. Francis, K. C. Seymour, W. M. Kriven and R. Raj, *J. Am. Ceram. Soc.*, 2015, **98**, 1493–1497.
15 J. M. Farley, J. S. Thorp, J. S. Ross and G. A. Saunders, *J. Mater. Sci.*, 1972, **7**, 475–476.
16 R. E. W. Casselton, *J. Appl. Electrochem.*, 1974, **4**, 25–48.
17 Y. Dong and I.-W. Chen, *J. Am. Ceram. Soc.*, 2018, **101**, 1058–1073.
18 R. Kirchheim, *Solid State Ionics*, 2018, **320**, 239–258.
19 X. Vendrell and A. R. West, *J. Electrochem. Soc.*, 2018, **165**, F966–F975.
20 C. Falgairette, C. Xia, Y. Li, W. Harbich, G. Foti and C. Comninellis, *J. Appl. Electrochem.*, 2010, **40**, 1901–1907.
21 J. Janek and C. Korte, *Solid State Ionics*, 1999, **116**, 181–195.
22 N. Ahr and M. Martin, *Solid State Ionics*, 2022, **386**, 116057.
23 M. Martin, P. Tigelmann, S. Schimschal-Thölke and G. Schulz, *Solid State Ionics*, 1995, **75**, 219–228.
24 A. Alvarez, Y. Dong and I. Chen, *J. Am. Ceram. Soc.*, 2020, **103**, 3178–3193.
25 B. LuerÃŸen, J. Janek, S. Günther, M. Kiskinova and R. Imbihl, *Phys. Chem. Chem. Phys.*, 2002, **4**, 2673–2679.
26 D. A. Siegel, F. El Gabaly, K. F. McCarty and N. C. Bartelt, *Phys. Rev. B: Condens. Matter Mater. Phys.*, 2015, **92**, 125421.
27 C. Rodenbücher, K. Szot, D. Wrana, B. R. Jany, F. Krok and C. Korte, *J. Phys.: Energy*, 2020, **2**, 034008.
28 V. R. PaiVerneker, *Phys. Rev. B: Condens. Matter Mater. Phys.*, 1989, **40**, 8555–8557.
29 P. MakuÅ‚a, M. Pacia and W. Macyk, *J. Phys. Chem. Lett.*, 2018, **9**, 6814–6817.
30 K. Szot, C. Rodenbücher, G. Bihlmayer, W. Speier, R. Ishikawa, N. Shibata and Y. Ikuhara, *Crystals*, 2018, **8**, 241.
31 M. Rogala, G. Bihlmayer, W. Speier, Z. Klusek, C. Rodenbücher and K. Szot, *Adv. Funct. Mater.*, 2015, **25**, 6382–6389.
32 K. Otsuka, A. Kuwabara, A. Nakamura, T. Yamamoto, K. Matsunaga and Y. Ikuhara, *Appl. Phys. Lett.*, 2003, **82**, 877–879.
33 Y. Saito, J. Cheng, K. Crabb, H. Huang, R. Pornprasertsuk, P. C. Su and F. Prinz, *ECS Trans.*, 2008, **11**, 3–8.
34 B. Feng, R. Ishikawa, A. Kumamoto, N. Shibata and Y. Ikuhara, *Nano Lett.*, 2019, **19**, 2162–2168.
35 Q. K. Muhammad, M. Scherer, A. K. Opitz, S. Taibl, C. Boehme, M. Rohnke, J. Janek, S. Gao, J. Fleig and T. Frömling, *ACS Nano*, 2022, **16**, 16655–16667.
36 B. Lafuente, R. T. Downs, H. Yang and N. Stone, *Highlights in Mineralogical Crystallography*, Degruyter, 2015, pp. 1–30.
37 C. Caspers, A. Gloskovskii, W. Drube, C. M. Schneider and M. Müller, *J. Appl. Phys.*, 2014, **115**, 17C111.
38 C. Rodenbücher, E. Hildebrandt, K. Szot, S. U. Sharath, J. Kurian, P. Komissinskiy, U. Breuer, R. Waser and L. Alff, *Appl. Phys. Lett.*, 2016, **108**, 252903.

© 2026 The Author(s). Published by the Royal Society of Chemistry